Title

Toward Optimal Photocatalytic Hydrogen Generation from Water Using Pyrene-Based Metal–Organic Frameworks

Journal

ACS Applied Materials & Interfaces, 13(48)

ISSN

1944-8244

Authors

Kinik, F Pelin
Ortega-Guerrero, Andres
Ebrahim, Fatmah Mish
et al.

Publication Date

2021-12-08

DOI

10.1021/acsami.1c16464

Peer reviewed

ACS APPLIED MATERIALS & INTERFACES

www.acsami.org

Research Article

Toward Optimal Photocatalytic Hydrogen Generation from Water Using Pyrene-Based Metal–Organic Frameworks

F. Pelin Kinik,[§] Andres Ortega-Guerrero,[§] Fatmah Mish Ebrahim, Christopher P. Ireland, Ozge Kadioglu, Amber Mace, Mehrdad Asgari, and Berend Smit*

Cite This: *ACS Appl. Mater. Interfaces* 2021, 13, 57118–57131

Read Online

ACCESS | Metrics & More | Article Recommendations | Supporting Information

ABSTRACT: Metal–organic frameworks (MOFs) are promising materials for the photocatalytic H_2 evolution reaction (HER) from water. To find the optimal MOF for a photocatalytic HER, one has to consider many different factors. For example, studies have emphasized the importance of light absorption capability, optical band gap, and band alignment. However, most of these studies have been carried out on very different materials. In this work, we present a combined experimental and computation study of the photocatalytic HER performance of a set of isostructural pyrene-based MOFs (M-TBAPy, where M = Sc, Al, Ti, and In). We systematically studied the effects of changing the metal in the node on the different factors that contribute to the HER rate (e.g., optical properties, the band structure, and water adsorption). In addition, for Sc-TBAPy, we also studied the effect of changes in the crystal morphology on the photocatalytic HER rate. We used this understanding to improve the photocatalytic HER efficiency of Sc-TBAPy, to exceed the one reported for Ti-TBAPy, in the presence of a co-catalyst.

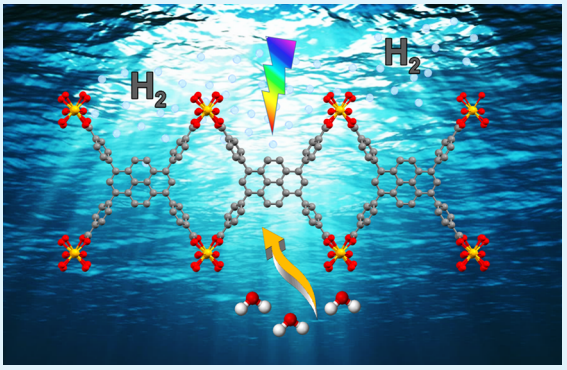

KEYWORDS: *metal–organic frameworks, photocatalysis, hydrogen evolution, pyrene, density functional theory*

INTRODUCTION

Metal–organic frameworks (MOFs) are crystalline materials consisting of metal-based building blocks linked by organic bridging ligands. The presence of the metal centers in their structure, their high porosity (facilitating the exposure of active sites), and their structural tunability allow MOFs to exhibit catalytic activity toward different reactions.[1−7] Photocatalytic H_2 evolution reaction (HER) from water is one of the promising catalytic applications that MOFs have been investigated for, thanks to their advantageous characteristics such as (i) adjustable light absorption, (ii) porous structure shortening the charge transfer path and improving the separation of electron–hole pairs, and (iii) possibility of incorporating different co-catalysts or photosensitizers to promote the separation of electron–hole pairs.[8−11] Depending on the design principles of MOFs, they can produce H_2 from water under UV or UV–visible light. The UV light irradiation conditions correspond to only 3–5% of the solar spectrum;[12] therefore, the development of visible-light active MOFs has been of importance by the careful selection of the ligand.

To design MOFs for photocatalytic HER from water, it is important to understand the factors that contribute to the overall performance. Similar to any photocatalytic material, the HER photocatalytic activity of a MOF relies on having a material with adequate light absorption capability, optical band gap, and band alignment.[13,14] In addition, Guo et al.[15] demonstrated that different morphologies of the same MOFs can have strikingly different performances. Nasalevich et al.[16] showed that MOFs having different electronic properties perform differently toward photocatalytic HER. However, the lack of a systematic study investigating all these effects together makes it difficult to compare the relative importance of these different factors. We believe that isostructural MOFs is a good platform for this investigation, thanks to their similar crystal structures.

In this work, we present a combined experimental and computational study on a family of pyrene-based isostructural MOFs. We systematically investigate different factors that contribute to the photocatalytic HER from water. In particular, we study (i) the effect of metal coordinated in the MOF, causing differences in the electronic and optical properties, and (ii) the effect of morphological characteristics. We show how these insights can be used to tune different factors that can be affecting the HER performance of MOFs and can be generalized to other photocatalytic MOFs.

Received: August 27, 2021
Accepted: November 12, 2021
Published: November 24, 2021

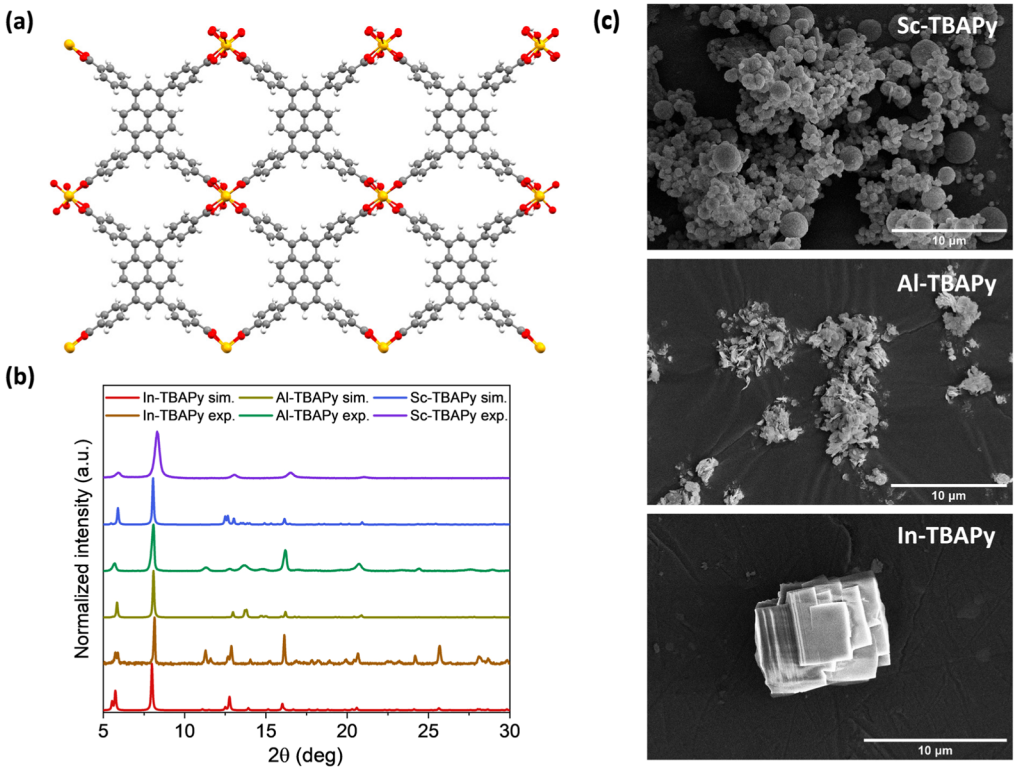

Figure 1. (a) Crystal structure of M-TBAPy (where M = Sc, Al, and In) MOFs. Color code: M: yellow, O: red, C: gray, and H: white. (b) PXRD patterns of isostructural M-TBAPy MOFs, showing a good match between the individual experimental and simulated patterns. (c) SEM images of Sc-TBAPy (top), Al-TBAPy (middle), and In-TBAPy (bottom), demonstrating different crystallite sizes and morphologies of the MOFs.

RESULTS

For our study, we compared the performance of HER for a family of isostructural pyrene-based TBAPy MOFs, which we refer to as "M-TBAPy" (M = Al, In, and Sc, Figure 1a). Pyrene exhibits favorable intense visible-light absorption, energy-transfer ability, and a long excited-state lifetime with successful electron hole-pair dissociation, which is the reason for the selection of TBAPy as the ligand.[17,18] AlPyrMOF[19] and ROD-7[20] were synthesized using the procedures from the literature. In this work, we refer to these two materials as Al-TBAPy and In-TBAPy, respectively. We synthesized the novel isostructural Sc version of the M-TBAPy MOFs, Sc-TBAPy (for more details, see "Material Synthesis and Characterization"). The framework of Sc-TBAPy is based on the chains of octahedral $ScO_4(OH)_2$ units, where each Sc(III) is bound to four TBAPy ligands and two μ_2 trans hydroxide anions (Figure 1a). Comparison of the simulated and experimental powder X-ray diffraction (PXRD) patterns show that for each of the three materials, we obtained the desired structure (Figure 1b). LeBail analysis of collected powder patterns for Sc-TBAPy, Al-TBAPy, and In-TBAPy was carried out using TOPAS 5 software (Figures S1−S3). The good agreement between experimental patterns and the constructed profile fits based on Le Bail analysis confirms the successful formation of the isostructural frameworks with *sea* topology,[20,21] for all three cases, as it was initially aimed for. Sc-TBAPy is found to be stable in different organic solvents for 48 h (Figure S5).

Scanning electron microscopy (SEM) images revealed that although the synthesis conditions for all three MOFs are the same [85 °C for 12 h in a mixture of dimethylformamide (DMF)/dioxane/H_2O], the metal has a pronounced effect on the crystal morphology. Sc-, Al-, and In-TBAPy form spherical crystals, circular discs, and intergrown rectangular plates, respectively (Figure 1c). The size of In-TBAPy crystals is an order of magnitude bigger than those of Al- and Sc-TBAPy. Sc-TBAPy has a broader particle size distribution compared to those of Al- and In-TBAPy. While the smaller crystals of Sc-TBAPy are in similar size with those of Al-TBAPy, the circular discs of Al-TBAPy are smaller than the bigger spheres of Sc-TBAPy crystallites.

Cadiau et al.[21] reported the synthesis of the Ti version, ACM-1, which we refer to as Ti-TBAPy. Our synthesis attempts for Ti-TBAPy were not successful, which we attributed to the complexity of Ti chemistry and its sensitivity to synthesis conditions to isolate crystalline Ti-MOFs.[22,23] As for Ti-TBAPy, detailed HER experiments have been reported; in our comparison of the different properties, we therefore used the data reported by Cadiau et al.

This family of M-TBAPy MOFs allows us to systematically study the effect of metal on the HER activity, thanks to them being isostructural. It should be highlighted that the comparison with metals (e.g., Zn, Ni, Ca, and Mg) that give different topologies would bring another variable to compare. Because isostructural M-TBAPy MOFs with Sc, Al, In, and Ti metals have the same topology and each of them has a TBAPy ligand, we could precisely explore the importance of metal selection on HER performance of the MOF. In addition, we investigate in detail how the metal impacts the different factors that contribute to the HER, such as the electronic structure of the MOF and the optical characteristics. The catalytic activity can be enhanced by a favorable interaction of the framework with water. Therefore, we investigated the effect of the metal coordination on the interaction between a water molecule and

https://doi.org/10.1021/acsami.1c16464
ACS Appl. Mater. Interfaces 2021, 13, 57118−57131

the MOFs by analyzing the preferred adsorption sites of water in M-TBAPy MOFs.

Photocatalytic Performances. The photocatalytic HER performances of Sc-, Al-, and In-TBAPy MOFs were investigated under visible-light irradiation using a 300 W Xe lamp, with a 420 nm cutoff filter to remove any UV light. Reactions were performed in the presence of triethylamine (TEA) as the sacrificial reagent. The same conditions (17 mg of MOF in 17 mL of photocatalytic solution in a 25 mL reactor, 3 h of reaction) were established for all MOFs for the comparability of the photocatalytic performances. Figure 2

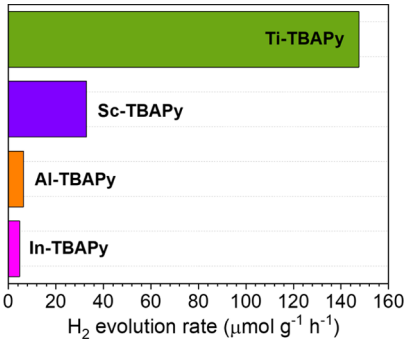

Figure 2. Photocatalytic HER rates of Sc-, Al-, and In-TBAPy MOFs under visible light irradiation ($\lambda \geq 420$ nm, 3 h reaction). Ti-TBAPy was included for comparison, where photocatalysis was conducted under visible light irradiation ($\lambda \geq 380$ nm, data from Cadiau et al.[21]).

shows that all three MOFs are capable of producing H_2 from water under specified conditions. The HER rates of In-TBAPy (4.7 μmol g^{-1} h^{-1}) and Al-TBAPy (6.3 μmol g^{-1} h^{-1}) are comparable, while Sc-TBAPy has a higher HER rate of 32.8 μmol g^{-1} h^{-1}. The HER rate of Sc-TBAPy was found to be less than that of Ti-TBAPy (147.5 μmol g^{-1} h^{-1}).[21] Our experiments are not done at exactly the same conditions with that of Ti-TBAPy, but these differences are not expected to change the ranking.

Electronic Characteristics. There can be different factors that can explain the effect of the metal on the photocatalytic HER performance. One of these factors is the position of the band edges with respect to the redox potential of water. A thermodynamic requirement is the proper alignment of the band edges of the materials with the reduction and oxidation potential for water splitting, that is, the conduction band minimum (CBM) being above the H^+/H_2 reduction potential for HER and the valence band maximum (VBM) below the H_2O/O_2 oxidation potential for oxygen evolution reaction.

To analyze the positions of these band edges of the M-TBAPy MOFs (M = Al, In, Sc, and Ti), we carried out density functional theory (DFT) calculations. In these calculations, we optimized the structures with the PBE0 functional using the *Cmmm* space group symmetry (see "Materials and Methods"). Figure 3 shows that for all materials, this requirement is fulfilled. The methodology to calculate the vacuum level consists of evaluating the average potential within a small sphere at the pore center of the MOFs. The alignment of the VBM in Ti-TBAPy is lower than in the other materials despite their similarities. This can be associated with the difference average potential due to the change in the coordination of the μ_2-OH groups in Al-, In-, and Sc-TBAPy MOF to μ_2-O in Ti-TBAPy. Our computations are carried out on ideal crystals; it would therefore be interesting to compare our predictions with

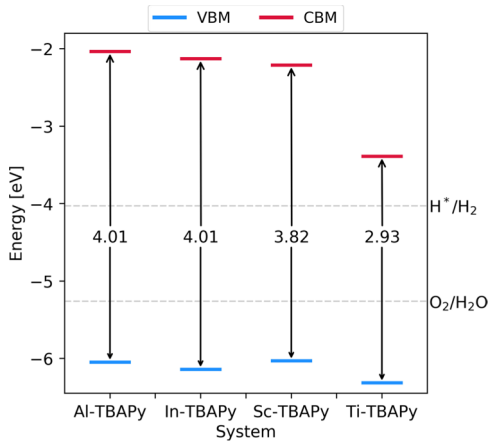

Figure 3. Energy diagrams of fundamental band gaps and the band edge positions with respect to the vacuum potential computed at the pore center for Al-TBAPy, In-TBAPy, Sc-TBAPy, and Ti-TBAPy. The dashed lines are redox potentials of water splitting.

some experimental analysis such as the Mott–Schottky curve or inverse photoemission spectroscopy. These experiments will determine the VBM and CBM, respectively. Both are necessary in the case of MOFs to properly capture the excitonic effects of MOFs. However, these techniques are either challenging[24] or not yet routinely applied to MOFs.[21] Therefore, it would indeed be interesting that these techniques would become available for MOFs.

Our DFT calculations also provide us with the band structures. From the shape of the band structure, we can obtain some insights into the photoconductive properties and the mobility of the charge carriers. Likewise, the effective mass of the carriers is proportional to the inverse of the electronic dispersion in the reciprocal space (curvature) at the band structure edges.[25] This effective mass is inversely proportional to the definition of the charge mobility according to the Bardeen–Shockley mobility model.[26] Therefore, the curvature of the CBM and VBM will be related to the mobility of the photoexcited electrons and holes, respectively. The flatter the shape of the band, the higher the effective mass, and as a high effective mass can be associated with a low charge mobility, such a flat shape can be associated with poor photoconductivity.

Figure 4 shows the band structure calculations of the different M-TBAPy MOFs (M = Sc, Al, In, and Ti) together with a visualization of the CBM and VBM orbitals. All MOFs show a similar flat band for the VBM, but for the CBM, we see a large effect of the metals. For Al-TBAPy and In-TBAPy, the CBM orbitals are located on the pyrene core of the TBAPy ligands, while for Sc-TBAPy and Ti-TBAPy these are localized along with the coordination complex, involving the metal and phenyl groups. For all four materials, the valence band is the result of the contribution of pyrene π orbitals; hence in these crystals, the VBM orbital is localized (Figure 4). The metals do impact the shape of the conduction band. Al-TBAPy and In-TBAPy have a flat band for the CBM and have the same band gap. For Al-TBAPy and In-TBAPy, the VBM and CBM are both localized on the π and π^* pyrene orbitals of the TBAPy ligands, respectively.[27] As the band gap for these materials is dominated by the pyrene orbitals of the ligand, the calculation will predict the same values for band gaps. In contrast, Sc-TBAPy and Ti-TBAPy have a CBM placed below the pyrene

https://doi.org/10.1021/acsami.1c16464
ACS Appl. Mater. Interfaces 2021, 13, 57118−57131

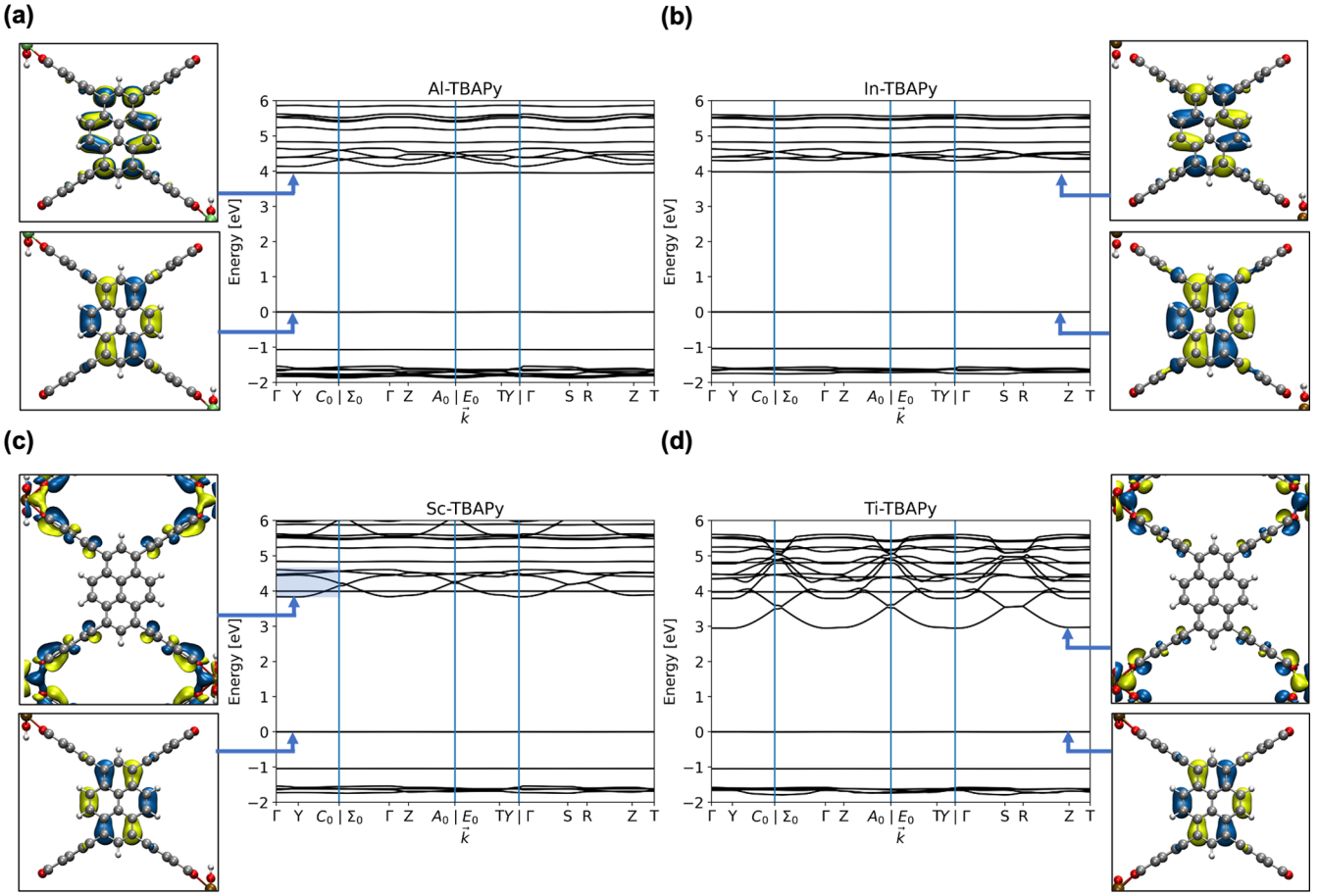

Figure 4. Band structure calculations and CBM and VBM crystal orbitals of the pyrene-based MOFs using the PBE0 functional with the *Cmmm* space group (symmetrical structure). (a) Al-TBAPy, (b) In-TBAPy, (c) Sc-TBAPy, and (d) Ti-TBAPy. The blue square highlights the conduction bands in Sc-TBAPy.

orbitals leading to smaller band gaps. Sc-TBAPy presents a slightly smaller band gap than Al and In-TBAPy MOFs because the CBM composed by orbitals of the Sc and phenyl groups is placed just below the pyrene orbitals (Figure 4c). The former are the ones associated with the one-dimensional Sc metal-rod-like structure form in the topology of the M-TBAPy MOFs. This leads to a CBM with more electronic dispersion in the reciprocal space. Ti-TBAPy has the smallest band gap of the four materials because its CBM is localized only in the Ti d-orbitals and it has a more pronounced dispersion among the four materials (Figure 4d).

Unlike Al- and In-TBAPy, Sc-TBAPy shows the proximity of other bands touching the CBM in different points of the reciprocal space (Figure 4c). This suggests that the Sc-TBAPy conduction band presents the contribution of different orbitals of the MOF. Figure S18a shows the contribution of the electronic density of states of the four materials around the band edges. Despite Sc-TBAPy, CBM shows the presence of Sc orbitals, and its contribution is minimal. This is not the case in Ti-TBAPy where the Ti orbitals contribute the most in the CBM. Likewise, Sc-TBAPy CBM presents a relatively small energy gap between the higher energy states (compared to Al- and In-TBAPy MOFs) as a result of its electronic dispersion.

In this scenario, the Ti-TBAPy (curved) band structure depicts a system with higher electron mobility among the four MOFs. In the case of Al-TBAPy and In-TBAPy, due to having a low dispersion (flat bands), and having carriers localized on the pyrene, carrier mobility is through a much slower hopping transport regime. In the case of Sc-TBAPy, its CBM presents less curvature than that of Ti-TBAPy, yet it suggests a better electron photoconductivity than its Al and In counterparts. The Sc-TBAPy conduction band suggests a better participation from the pyrene and the Sc metal-rod orbitals (i.e., π^*-orbitals of the benzoic acid fragment of the ligand and d-orbitals of Sc metal) in the mobility of the photogenerated electrons. However, the contribution of Sc orbitals in the CBM is small unlike the case of Ti-TBAPy, where the Ti d-orbitals present most of the contribution (Figure S18a). The above depicts ligand to metal charge transfer (LMCT) in the case of Ti-TBAPy, as it was reported by Cadiau et al.[21]

Sc-TBAPy is particularly interesting from a theoretical point of view because of the proximity of the CBM to the orbitals of the pyrene ligand. This proximity makes the calculations very sensitive to the exact orientation of the phenyl groups in the ligands.[28] The optimized ground-state structure of Sc-TBAPy is with high symmetry. We conducted vibrational frequency calculation on Sc-TBAPy, where the vibrational mode of the phenyl rotations has a vibration temperature of 48.9 K. Figure S19 shows the energy as a function of the orientation of the phenyl groups by scanning the geometry along this vibrational mode. To investigate the effect of the rotation of the phenyl groups on the electronic structure, we conducted PBE0 geometrical relaxation calculation on all four M-TBAPys in both the symmetric and the rotated position of the phenyl

https://doi.org/10.1021/acsami.1c16464
ACS Appl. Mater. Interfaces 2021, 13, 57118−57131

rings. We refer to these as "symmetrical" and "rotated", respectively. Sc-TBAPy has a local minimum, with an energy that is slightly higher than the ground state. In this local minimum, the phenyl groups have a rotation angle of 8°. The energy barrier between the ground state and this local minimum is relatively low (≈3.35 meV). Therefore, it can be expected that because of the thermal fluctuations, the phenyl groups can be found in both orientations.

Figures 4 and S16 show the band structures of the symmetrical and rotated systems, respectively. For Al- and In-TBAPy systems, we see that the rotated case causes the CBM orbital to be at a lower energy. The rotation changes the localization of the pyrene core orbitals, causing the π^*-orbitals to move down, and hence, we see a small decrease in the band gap. As for Ti-TBAPy, the CBM is dominated by the orbitals on Ti, and these rotations of the phenyl group have therefore little impact. In contrast, Sc-TBAPy around the CBM, there are contributions from both the ligand as well as the metal orbitals. In the rotated case, the CBM is localized on the π^* orbital of the pyrene ligand and the Sc metal orbitals lie above, but in the symmetric case, this description was the opposite (see Figures 5 and S15). If we now take the thermal fluctuations (or the presence of solvent, see Figure S17) into account, then the CBM of Sc-TBAPy consists of contributions from both the orbitals on the Sc-rod and the π^* pyrene orbitals. This result suggests that the probability of Sc-rod crystal orbital states being populated in the excited-state dynamics of the Sc-TBAPy system is higher than in the Al- and In-counterparts, given their proximity to the pyrene orbitals.

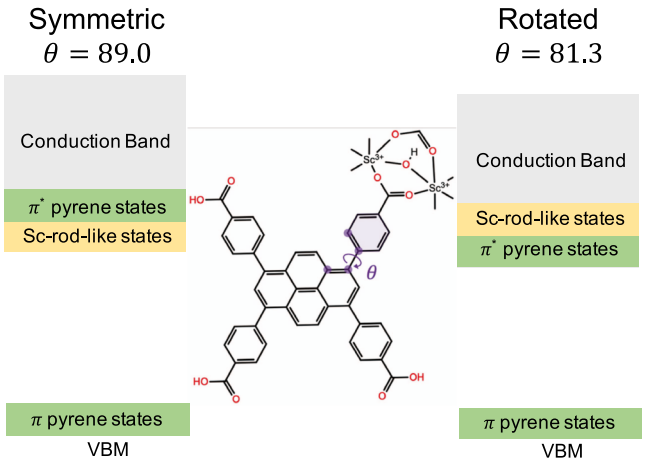

Figure 5. Representation of the different characters of the valence band and conduction band edges in Sc-TBAPy for the symmetric and rotated structures. The rotation angle (Θ) of the phenyl group is represented as the dihedral between the four highlighted carbon atoms.

Because Sc-TBAPy CBM contains contributions from both the ligand as well from the Sc orbitals, it is important to establish whether the mechanism of the optical excitations is LMCT, ligand-centered (LC), or both. For this, we first computed the optical band gap (or the first optical excitation) of the four materials to establish the nature of the optical transition. For these calculations, we use linear-response time-dependent DFT (LR-TDDFT). Table 1 shows the values of the ground state and optical band gaps in both the symmetric and rotated cases. It can be seen that in Al-, In-, and Sc-TBAPy MOFs, the nature of the optical band gap is the $\pi-\pi^*$ optical transition (LC transition). The rotated cases present smaller optical band gaps than the symmetric cases, keeping the same behavior as the one described before for the ground-state band gaps. Although the symmetric case of Sc-TBAPy has a CBM with a contribution of the Sc orbitals, the first optical transition is associated with a LC transition despite the pyrene orbitals being higher in energy. This is a result of the excitonic effects (originated from the electron−hole Coulombic interactions) in MOFs.[29] On the other hand, Ti-TBAPy's first excitation is an LMCT excitation from the pyrene to the Ti orbitals, as it was reported as well by Cadiau et al.[21] The experimental measurement of the optical band gaps in Al-, In-, and Sc-TBAPy MOFs was determined via Tauc plots (see Figure S6). The experimental optical band gaps are 2.68, 2.63, and 2.58 eV for Al-TBAPy, In-TBAPy, and Sc-TBAPy, respectively. The optical band gap values obtained via LR-TDDFT are higher than the experimental values. The theoretical optical band gaps for the symmetric and rotated models are 0.7 and 0.5 eV higher than the experimental optical band gap values, respectively. Although this difference can appear significant, it is noteworthy to mention that the experiments are performed at room temperature, while our calculations are performed at 0 K. Our calculations do not consider the thermal effects and the quantum motion of the nuclei contributions on the band gap. The inclusion of these effects has shown a decrease in the calculated band gaps and better agreement with experiments.[30] On the other hand, Ti-TBAPy can suffer the limitations of using the PBE0 functional. Such a limitation is expected given the difficulties of LR-TDDFT for describing the optical transition energies in charge-transfer states when using pure hybrid functionals.

We also investigated the possibility of Sc-TBAPy trapping an electron in the Sc orbitals in the form of a polaron. For this, we added an electron to our system and we computed the interactions of this extra electron with the material (i.e.,

Table 1. Comparison between the Theoretical Ground State E_{gs} and Optical E_{opt} Band Gaps and the Experimental Optical Band Gaps E_{exp}[a]

	symmetric			rotated			
system	E_{gs} (eV)	E_{opt} (eV)	transition[b]	E_{gs} (eV)	E_{opt} (eV)	transition[b]	E_{exp} (eV)
Al-TBAPy	4.01	3.40	LC	3.76	3.18	LC	2.68
In-TBAPy	4.01	3.41	LC	3.72	3.14	LC	2.63
Sc-TBAPy	3.82	3.40	LC	3.77	3.21	LC	2.58
Ti-TBAPy	2.93	2.86	LMCT	2.94	2.82	LMCT	2.30[c]

[a]The calculations are conducted using the symmetrical and phenyl rings rotated structures with the PBE0 exchange−correlation functional. The nature of the optical transition excitations is included as well. [b]LC stands for "ligand-centered" transition and LMCT stands for "ligand to metal charge transfer". [c]Data from Cadiau et al.[21]

https://doi.org/10.1021/acsami.1c16464
ACS Appl. Mater. Interfaces 2021, 13, 57118−57131

electron polaron) in the four materials. Polarons can appear because of doping or charge injection or be created through the separation of an exciton formed through electronic excitation.[31] We considered the calculation of the symmetric and the rotated structures of the M-TBAPy MOFs. The polarons are localized in their respective CBM orbitals: π^* pyrene orbitals for Al- and In-TBAPy, and the d-orbital of a Ti atom in Ti-TBAPy (Figure S20). The electron polarons of Al-, In-, and Ti-TBAPy MOFs are not affected by the presence of the phenyl rotations. For Al and In, the polaron is trapped on the ligand, hence a LC transition. For Ti, the electron polaron trapping on the d-orbitals of the metal leads to a Ti(III) oxidation and hence an LMCT mechanism. Sc-TBAPy presents an electron polaron localized in the π^* pyrene orbitals for the rotated structure (Figure S20c) and in the Sc and phenyl orbitals from the rod in the symmetric structure (Figure S21b). The latter resulted in a more delocalized electron polaron given the crystal orbital and the dispersion of the band structure. The Mulliken charge distribution analysis indicates that even in the symmetric case there is no electron trapping on the Sc atoms leading to an Sc(II) oxidation state, discarding the possibility of LMCT for both the symmetric and rotated case.

From our electronic structure calculations, we can conclude that Sc-TBAPy and Ti-TBAPy coordination promotes a better CBM dispersion. In the case of Ti, LMCT leads to beneficial electronic properties for HER than the ones with Al and In. Sc-TBAPy's electronic properties are different from the other isoreticular M-TBAPy MOFs due to the presence of the ligand as well as the metal orbitals near the CBM which lead to a better electron mobility compared to Al- and In-TBAPy.

Optical Characteristics. For the photocatalytic activity, it is important that the MOFs absorb light at the desired frequencies. The differences between the M-TBAPy MOFs in terms of their light absorption can be seen from the diffuse reflectance ultraviolet−visible (UV−vis) spectra shown in Figure 6. The UV−vis spectra of Al-TBAPy exhibit a broad

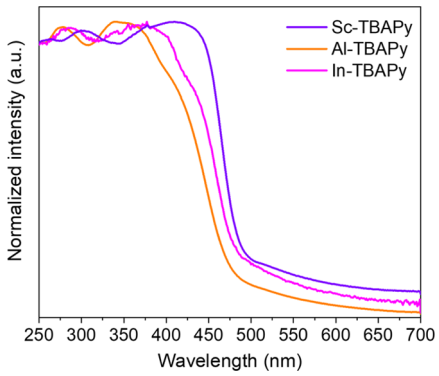

Figure 6. UV−vis spectra of M-TBAPy MOFs.

light absorption ranging from 250 to 475 nm, with two main peaks at 278 and 350 nm. The absorbance maxima are red-shifted for both In-TBAPy (375 nm) and Sc-TBAPy (415 nm) compared to that of Al-TBAPy at 350 nm. This result shows that Sc-TBAPy absorbs better in the visible light region than the other two MOFs, which contributes to its better HER rate. Although the absorption maxima of Ti-TBAPy is similar to that of Sc-TBAPy, its visible light absorption is slightly extended (up to ≈550 nm)[21] than that of Sc-TBAPy (up to ≈500 nm).

Whereas the absorption spectra give us information on which photons are absorbed, the apparent quantum yields (AQYs) give us a fraction of photons arriving on the sample that cause a chemical reaction to take place.[32] The AQYs of Al-TBAPy and Sc-TBAPy were measured by ferrioxalate actinometry at 400 and 450 nm, respectively (Table S1).[33−35] While both MOFs showed similar AQY yields at 400 nm irradiation (≈0.076%), Sc-TBAPy showed better AQY (0.364%) compared to that of Al-TBAPy (negligible) at 450 nm.

Another important quantity for the analysis of the efficient HER is the lifetimes of the photoexcited electrons. Therefore, we performed time-resolved photoluminescence measurements to record the duration of the decay of the photoexcited electrons. The photoluminescence lifetimes of Sc-, Al-, and In-TBAPy show two decay features, with the longer lifetime (t_2) feature corresponding to the decay localized on the pyrene core, and the shorter lifetime (t_1) corresponding to the rotation of the phenyl rings.[36] Table S3 shows that Sc-TBAPy has a shorter photoluminescence lifetime [(t_1) = 2.40 and (t_2) = 11.70 ns] than its Al [(t_1) = 2.72 and (t_2) = 13.42] and In [(t_1) = 2.84 and (t_2) = 12.18 ns] counterparts. The shorter lifetime of Sc-TBAPy can be attributed to the localization of the CBM around the phenyl rings and Sc rods rather than on the pyrene core, resulting in an overall shorter-lived excited state.[36] These results present an interesting example of the complexity of photocatalytic HER. If we would only consider the photoluminescence lifetime, one would conclude that those MOFs with the long photoluminescence lifetimes are those with an efficient charge separation and are thus often directly linked to better HER performance.[21,37,38] The case of Sc-TBAPy, however, demonstrates that different mechanisms can propose different explanations for lifetimes.

To gain further insights into the mechanism that causes these differences in photoluminescence lifetimes, we carried out nanosecond transient absorption spectroscopy (nTAS) analysis. nTAS is a pump−probe technique which is used to measure dynamic changes in the absorption of a photoexcited sample.[39] A broad-spectrum probe light illuminates the sample at nanosecond time intervals, before and after it has been photoexcited by a pump pulse. By plotting the difference in the sample's absorbance before and after photoexcitation as a function of wavelength and time, we gain insights into the dynamics of photoexcited charge carriers. For example, as molecules are promoted to the excited state through the pump pulse, the number of ground-state molecules decreases. Consequently, the ground-state absorption in the excited sample is less than that in the nonexcited sample. This creates a negative signal in the absorption spectrum, which is known as ground-state bleach (GSB).[39] Figure 7a−c shows the GSB of M-TBAPy MOFs at the two absorption bands, around 300 and 500 nm. As expected, the shape of the GSB reflects the steady-state UV−vis absorption spectra of the MOFs, with Sc-TBAPy exhibiting a broad single peak from 450 to 550 nm and In- and Al-TBAPy exhibiting slightly blue-shifted peak maxima around 425 nm and a broad shoulder above 450 nm. The GSB recovery of the three MOFs matches their photoluminescence lifetimes, with Sc-TBAPy having the shortest recovery, followed by In-TBAPy and then Al-TBAPy.

A key characteristic of the In- and Al-TBAPy nTAS profiles, in particular, is the clear red-shifting of the principal 425 nm peak with time, indicated by the black arrows in Figure 7b,c. Such a redshift is typically indicative of nonradiative, vibrational losses, from the higher vibrational S_1 energy states

https://doi.org/10.1021/acsami.1c16464
ACS Appl. Mater. Interfaces 2021, 13, 57118−57131

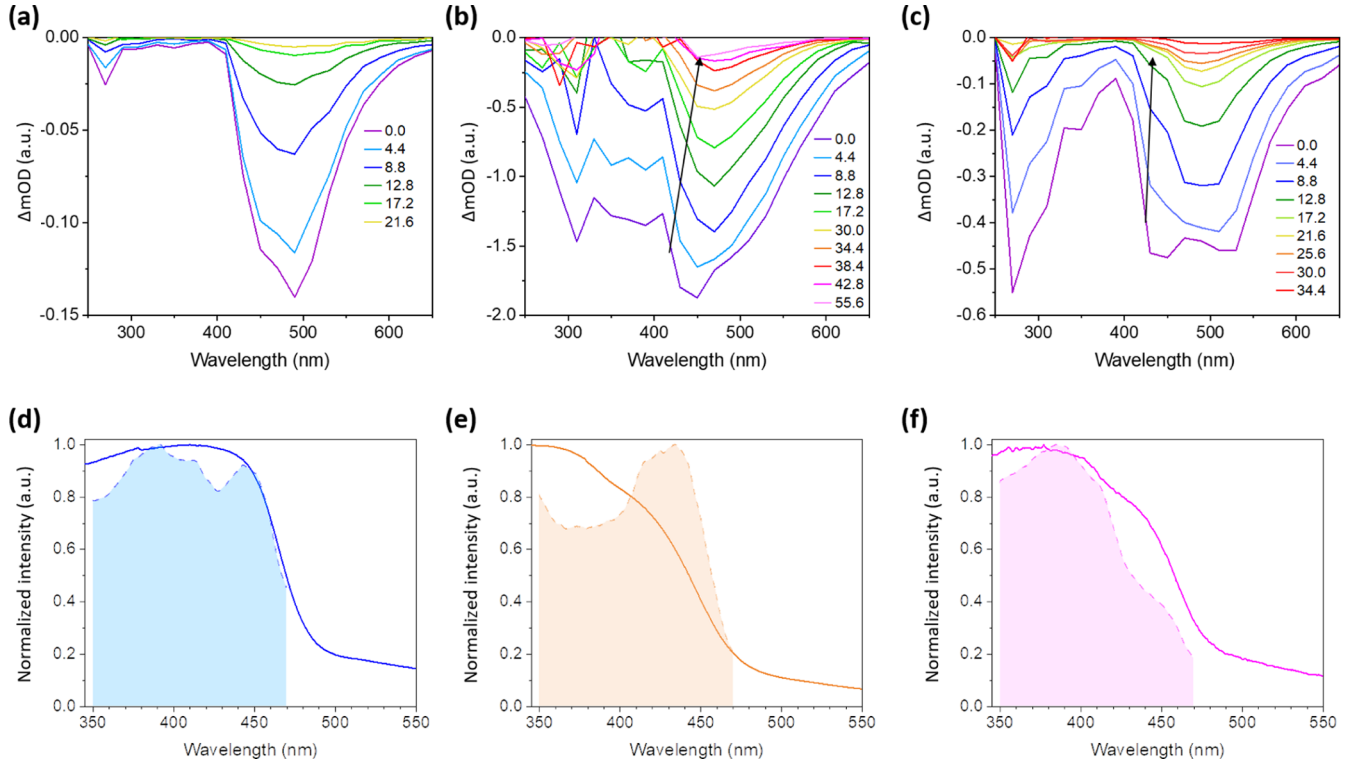

Figure 7. Upper panel: nTAS of (a) Sc-TBAPy, (b) Al-TBAPy, and (c) In-TBAPy (upon excitation at 420 nm). Lower panel: steady-state UV−vis absorption spectra (solid lines) and excitation spectra (shaded regions) of (d) Sc-TBAPy, (e) Al-TBAPy, and (f) In-TBAPy.

to the CBM, which lower the energy of the excited state with time, and are typically seen in photoexcited pyrene.[40,41] In the case of Al-TBAPy and In-TBAPy MOFs, the transient redshift can be seen over a longer timescale than what is typically observed due to vibrational decays.[40] This is likely due to interligand interactions in the Al- and In-TBAPy MOFs. Because the CBM in both these structures is localized on the pyrene core, it is expected that electrons from adjacent pyrene cores will interact in the excited state to form excimers.[36,42] The decay of these excimers presumably adds a long lifetime component to the vibrational redshift of the GSB. We can therefore conjecture that while localization of the CBM on the phenyl rings in Sc-TBAPy results in a shorter lifetime and a single prominent feature in its transient and steady-state absorption spectra, the distribution of charges around the pyrene core in In- and Al-TBAPy accounts for their longer excited-state lifetimes and the distinct vibrational features in their TAS profiles.

Comparing the UV−vis absorption of the three MOFs with their respective excitation spectra further supports the hypothesis that Al- and In-TBAPy suffer from more non-radiative, vibrational losses than Sc-TBAPy.[36] As seen in Figure 7d−f, when probing the 500 nm emitting S_1 state, the excitation spectrum of Sc-TBAPy (shaded region) closely follows its UV−vis absorption spectrum (solid line). This suggests that absorbed photons are efficiently populating on the S_1 excited state of the MOF. This is less evident in In- and Al-TBAPy, where a discrepancy between the absorption profiles and excitation spectra suggests that a portion of photoexcited electrons are undergoing vibrational decay.

Studies of pyrene suggest that the vibrationally unrelaxed state of pyrene molecules tends to be the active state for energy or charge transfer to a nearby acceptor.[40,43] Therefore, the absence of vibrational features in the Sc-TBAPy spectra implies that its photoexcited electrons are maintained in a vibrationally unrelaxed state, where they are in an energetically favorable position for water reduction. The combination of enhanced absorption, spatial localization of the CBM, and efficient photoexcitation of the active excited state all contribute to the superior performance of Sc-TBAPy as a photocatalyst. Our optical investigation thus highlights these three critical points: (i) LMCT is beneficial for charge-separation in MOFs, yet its absence is not a limiting factor for promising rates of HER, (ii) photoluminescence lifetime is not the only decisive parameter for photocatalytic HER, and distribution of charges in the MOF structure should be also considered, and (iii) vibrational losses due to the localization of charges in the core of TBAPy may depopulate the active state for water reduction in photocatalytic active pyrene MOFs.

Investigation of Interaction with Water. The interaction between water and the MOFs is an important parameter to consider for understanding HER activity because the differences in the adsorption of water could influence the effective kinetics of the HER. To comprehend this relationship, each M-TBAPy MOF was studied with classical molecular dynamics (MD) simulations (See "Computational Details"). Our electronic structure calculations depicted the importance of considering the rotation of the phenyl groups in the MOFs. Therefore, we carried out MD simulations with a fully flexible MOF. Because many classical simulations of guest particles adsorbed in a MOF assume that the MOF is rigid,[44,45] for comparison, we also carried out some MD simulations with a rigid model of the MOF.

Free energy isosurfaces of water were computed from the trajectories collected from the MD simulations. From these isosurfaces, we can obtain the probability of finding a water

https://doi.org/10.1021/acsami.1c16464
ACS Appl. Mater. Interfaces 2021, 13, 57118−57131

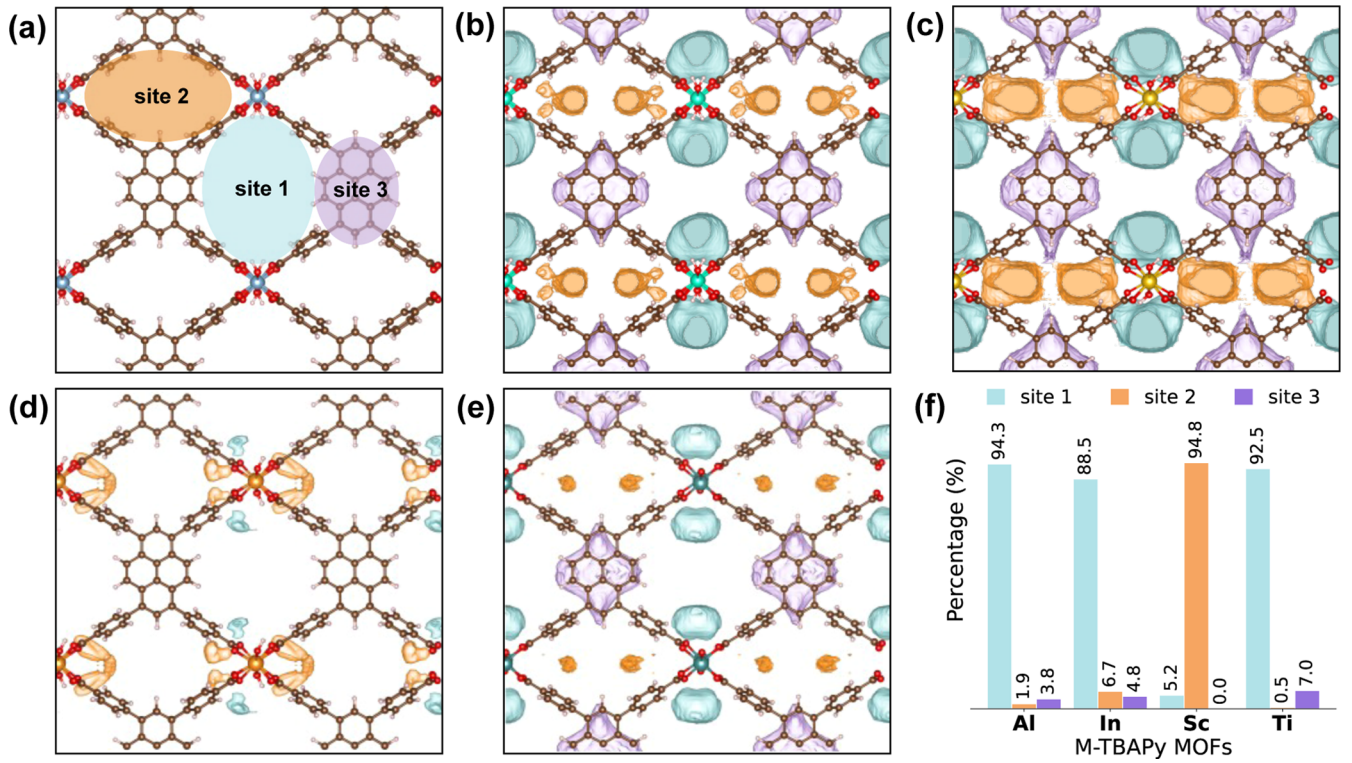

Figure 8. Free energy isosurfaces (15 kJ/mol) from the view of *x*-direction computed in DFT optimized (b) Al-TBAPy, (c) In-TBAPy, (d) Sc-TBAPy, and (e) Ti-TBAPy at 298.15 K. Turquoise, purple, and orange surfaces are the energy grids corresponding to the oxygen atoms in water represent the binding sites in the large pore (site 1), small pore (site 2), and in between pyrene stackings (site 3), respectively. Colored spheres in (b−e) correspond to the following atoms: C: brown; O: red; H: white; and Al, In, Sc, and Ti: cyan, orange, yellow, and blue, respectively. (f) Probabilities of finding a water molecule at the three different adsorption sites. Colors in the legend indicate the adsorption sites. All water distributions were computed with flexible frameworks.

molecule at a particular position in the MOFs. In Figure 8, we show the isovalue of 15 kJ/mol. From these plots, we identified three distinct adsorption sites in M-TBAPy MOFs. They are represented as site 1 (turquoise), site 2 (orange), and site 3 (purple), which show the large pores, small pores, and in between pyrene stackings, respectively (Figure 8a). From the free energy surfaces, it can be seen that water in Al-, In-, and Ti-TBAPy MOFs has a preference for the large pore (site 1), while water prefers the small pore (site 2) for Sc-TBAPy. What we also observe is that for both Ti- and Sc-TBAPy, the size of the surface is smaller, and hence, there is a more localized binding. To quantify these observations, we computed the probability of finding a water molecule at these three different binding sites. Figure 8f shows that water distribution is quantitatively similar for Al-, In-, and Ti-TBAPy, as the larger pore (site 1) is the most probable adsorption site for all. Sc-TBAPy water distribution stands out with its most preferential adsorption site being in the smaller pore (site 2) and zero probability of finding water between the pyrene stackings (site 3).

From the two-dimensional representation of the free energy (Supporting Information, Figure S23), we can link the more localized water distribution in Sc-TBAPy to deeper energy wells close to the metal node relative to other accessible regions, and thus, a higher probability of being close to the metal node. This can also be seen from the O−H radial distribution functions (Supporting Information, Figure S24), showing that the hydrogen bond formation between the water hydrogen and carboxylic oxygen is much more probable than in all other structures. This stronger interaction can be explained by the difference of the partial charges between the M-TBAPy MOFs (Supporting Information, Table S4). Sc has the most positive atomic partial charge of the four metals. This results in a more negative charge of the charge balancing oxygen surrounding the metal and thus results in stronger electrostatic interactions between the positively charged water hydrogen and the carboxylic oxygen of Sc-TBAPy, relative to all other structures.

Furthermore, the fact that Ti-TBAPy MOF does not have a hydroxyl group coordinated in the metal node will create a different geometry and chemical environment in site 1. From the radial distribution functions between the water hydrogen and the carboxylic oxygen (Figure S24), we see that the interactions are more probable in this environment relative to that of Al- and In-TBAPy MOFs. By looking at the trajectories, we observe that the interactions at this site in Ti-TBAPy are dominated by a bridged adsorption where both hydrogen atoms of the water molecule are interacting with two of the carboxylic oxygen simultaneously, which keeps the water more localized at this site. This is not observed in the structures where the hydroxyl group is present.

The near zero probability of finding water between the pyrenes in Sc-TBAPy can be explained by the strong adsorption at site 2 and the large difference in the free energies between sites 2 and 3. From Figure S23 (Supporting Information), we see that this free energy difference is 15−20 kJ/mol in this structure. This results in a negligible relative probability in the case of a single water molecule. For all other structures studied, the strongest adsorption is at site 1 and the free energy differences between sites 1 and 3 are in the range

https://doi.org/10.1021/acsami.1c16464
ACS Appl. Mater. Interfaces 2021, 13, 57118−57131

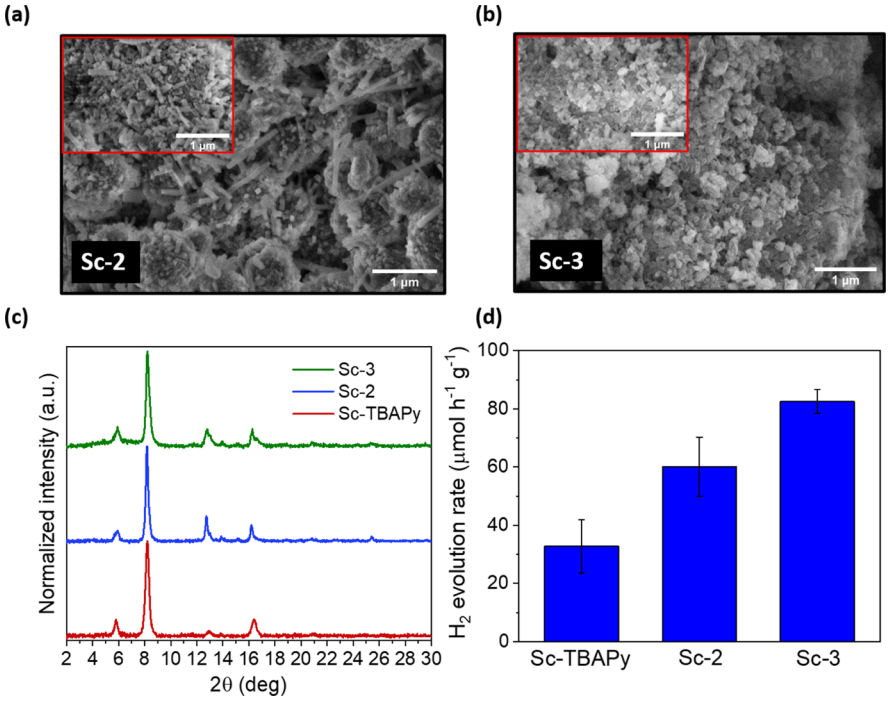

Figure 9. SEM images of (a) Sc-2 and (b) Sc-3 MOFs. (c) PXRD patterns of Sc-2 and Sc-3, showing that all three samples have the same crystallographic identity. (d) Photocatalytic HER rates of Sc-TBAPy, Sc-2, and Sc-3. Error bars represent the standard deviation of measured rates.

10−15 kJ/mol, which gives a slightly higher probability of finding the water between the pyrene stackings.

In Figure S22, we compare the free energy surfaces of Al-TBAPy with the results from a rigid model. This figure illustrates the importance of the flexibility of the MOFs, and in the rigid case, the water molecule cannot approach the metal site, while in the flexible case, the rotation of the phenyl ring opens up the adsorption site next to the metal. Also, the overall probability of finding the water molecules at the different sites is completely different.

For all structures, the MD study indicates a preference for the water molecule to be found near the metals of the MOFs. This result is potentially beneficial for the HER if the metal-coordinated clusters are involved in the reaction. Our water study highlights the impact of having Sc coordinated in M-TBAPy for a stronger interaction of water with the metal rod. In MOFs, photocatalytic HER can involve the participation of the metal atoms from the metal nodes.[46] In experimental conditions, this can be attributed to the presence of dangling bonds, defects, and exposed metal atoms on the external surface of the MOF crystal. We believe that the high probability of Sc-TBAPy having water near the metal clusters and the localized interactions between water and the rod of Ti-TBAPy benefit the electron transfer and HER reaction. Nevertheless, a key aspect to consider is the effect of the sacrificial agent. We used TEA as a sacrificial reagent because it has remarkable benefits in MOFs.[47] The performance of HER in MOFs is also affected by the ability of the sacrificial reagent to donate electrons, reducing electron−hole recombination. A more comprehensive study involving the study of sacrificial reagents with respect to MOFs is necessary. Likewise, different reagents can present distinctive photochemical reaction pathways and their theoretical and experimental study is challenging because it involves phenomena in the dynamics of the excited states.

Investigation of Morphological Characteristics. Our findings showed that the combination of its electronic and optical characteristics made Sc-TBAPy favorable toward photocatalytic HER compared to its Al and In counterparts. Nonetheless, it should be kept in mind that the structural characteristics should not be neglected when exploring the photocatalytic activity of MOFs.[15,48] Sc-TBAPy was selected as the case study and different syntheses conditions were applied to obtain different morphologies.

A structure-capping surfactant [cetyltrimethylammonium bromide (CTAB)] was used during the syntheses to allow the formation of different morphological characteristics.[15] It was observed that when the synthesis temperature was increased to 120 °C and the synthesis was performed for 72 h, the spherical particles of Sc-TBAPy (size of crystals ranging between 0.5 and 2.5 μm) were evolved to rectangular rods (named as "Sc-2", Figure 9a, size of crystals ranging between 0.25 and 0.5 μm). When the same synthesis condition for Sc-2 was performed in the absence of the modulator (HNO_3), smaller rectangular-shaped crystals were obtained (named as "Sc-3", Figure 9b, size of crystals ranging between 70 and 120 nm). PXRD patterns showed that Sc-2 and Sc-3 have comparable patterns to that of Sc-TBAPy (Figure 9c). Light absorption characteristics of Sc-TBAPy samples were investigated by UV−vis spectroscopy, demonstrating that all three materials have similar visible-light absorption (Figure S13).

Sc-2 and Sc-3 samples were investigated as photocatalysts for HER using the same photocatalytic conditions as mentioned before. Sc-3 performed the highest hydrogen evolution rate (82.5 μmol g^{-1} h^{-1}), followed by Sc-2 (60.6 μmol g^{-1} h^{-1}) and Sc-TBAPy (32.8 μmol g^{-1} h^{-1}) (Figure 9d). Catalytic activity of MOFs can be directly related to the catalyst size where MOFs with the smallest sizes can tend to exhibit superior photocatalytic performance.[49,50] Previous studies showed that the fraction of catalytic sites on edges and corners mainly determines the electron transfer efficiency,

https://doi.org/10.1021/acsami.1c16464
ACS Appl. Mater. Interfaces 2021, 13, 57118−57131

where smaller particles have higher density of these sites.[49,51] The shape and the facet of MOFs exposed to the catalysis is another important parameter.[15,48,52] Therefore, the better performance of Sc-3 might be attributed to its smallest size among all Sc-TBAPy MOFs. Moreover, the exposed facet of Sc-3 to the photocatalytic HER is possibly more favorable for H_2 generation from water compared to those of Sc-TBAPy and Sc-2. All these results show that the morphology can be as important as the electronic and optical characteristics in terms of photocatalytic activity; therefore, it should not be neglected when optimizing the reaction parameters.

CONCLUDING REMARKS

In this study, we synthesized a new TBAPy-based MOF with Sc(III) metal centers, which is isostructural to previously reported Al-, In-, and Ti-TBAPy MOFs. Sc-TBAPy performs a better photocatalytic HER rate (32.8 μmol g^{-1} h^{-1}) compared to its Al and In counterparts (6.3 and 4.7 μmol g^{-1} h^{-1}, respectively). Our ab initio calculations showed that there are some distinctions in the band alignments and band structures of M-TBAPy MOFs. Sc-rod orbitals are found to be located in the CBM in Sc-TBAPy, unlike the cases of its Al and In counterparts, where the CBM is localized on the pyrene orbitals. Interestingly, it was found that the vibrational rotations of the phenyl groups in TBAPy can modify the nature of the CBM in Sc-TBAPy. Our calculations indicated that Sc and Ti metals promote a better electron dispersion around the CBM in the band structure. Optical investigations demonstrated that Sc-TBAPy has an extended visible light absorption compared to Al- and In-TBAPy. nTAS measurements combined with the UV−vis absorption and the respective excitation spectra inferred that Al- and In-TBAPy suffer from more nonradiative, vibrational losses than Sc-TBAPy. Along with the electronic and optical investigation, morphological characteristics of Sc-TBAPy were modified to optimize the HER performance. With the optimized synthesis conditions of Sc-3, it is possible to increase the HER rate to 82.5 μmol g^{-1} h^{-1}.

Different chemical and structural factors come together to determine the photocatalytic HER rates of MOFs. Our study has addressed the understanding of various aspects and these are linked with the HER performances of M-TBAPy MOFs. The isoreticular nature of the selected M-TBAPy MOFs allowed us to explore the impact of using different metal elements on the resulting properties of MOFs. Our electronic structure investigation, optical characterization, and photocatalytic HER rates confirm how Sc-TBAPy excels among Al- and In-TBAPy. Likewise, our water interaction studies depicted the effect of having Sc and Ti coordinated in the M-TBAPy MOFs where the preferential adsorption site for water is near the metal site, which can be beneficial to the HER.

A key factor in the HER performance of the materials was the morphological study. Sc-TBAPy performance was improved considerably by the modification of the shape of the Sc-TBAPy crystals. A similar observation was described by Guo et al.,[15] where the change of morphology of MIL-125 crystals led to higher HER rates. Such enhancement was ascribed primarily to the exposure of specific facets of the crystals. This finding signifies the importance of controlled synthesis conditions for the desired morphological characteristics, which can be impactful for photocatalytic HER efficiency.

The main motivation of this work was to obtain a systematic understanding of the different factors that contribute to the HER. It is therefore interesting to see if we can use this knowledge to improve the catalytic performance of these MOFs. The most interesting case is Sc versus Ti. Our study shows that Sc-TBAPy has the potential to be a good HER catalyst but the most likely bottleneck is that the electrons do not reach the water molecules as efficiently as for Ti-TBAPy. A solution to this would be the addition of a co-catalyst. A co-catalyst can attract the excited electrons and reduce the possibility of electron−hole recombination. To test this hypothesis, we combined Pt nanoparticles with the different morphologies of the Sc-TBAPy. We observed that the photocatalytic HER rate of Sc-MOFs can be improved further by their combination with Pt nanoparticles. When Sc-3 was combined with 3 wt % Pt, the HER rate was increased to 3164 μmol g^{-1} h^{-1} (Figure 10) and the HER rate even exceeded that

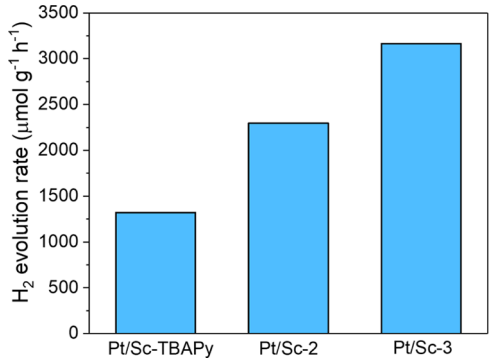

Figure 10. Photocatalytic HER rates of Sc-TBAPy, Sc-2, and Sc-3 in the presence of 3 wt % Pt co-catalyst, showing the improvement in the photocatalytic activity compared to bare MOFs. It can be deduced that the excited electrons are efficiently trapped by the Pt co-catalyst, increasing the HER rate.

of Pt/Ti-TBAPy (1675 μmol g^{-1} h^{-1}).[21] Although we have an activity that is almost a factor of 2 higher than for Pt/Ti-TBAPy, one has to be careful as these two studies have not been performed at exactly the same conditions. Also, for Ti-TBAPy, one could expect that changes of the morphology may give higher rates. Nevertheless, it is encouraging to see how our systematic study can show the way on how to improve the catalytic performance of a material that initially (see Figure 9) did not look that promising compared to Ti-TBAPy.

We believe that our strategy can be translated to the investigation of other efficient MOFs for photocatalytic HER studies. The exploration of the morphological and electronic properties is of great interest for this proposal hence there is a need for combining such studies. Likewise, the selection of isoreticular MOFs allowed us to explore the effect of different metals, yet this investigation should be extended to different ligands, which can potentially eventuate new MOF chemistry. Based on our observations, we can envision future efforts to have facet-controlled growth of MOF crystals as well as the interaction study with different co-catalysts for the optimization in photocatalytic HER applications.

MATERIALS AND METHODS

Material Synthesis and Characterization. The synthesis of the 4,4′,4″,4‴-(pyrene-1,3,6,8-tetrayl)tetrabenzoic acid (TBAPy) ligand was performed based on the previously reported procedure.[53] Al-TBAPy and In-TBAPy were synthesized according to the synthesis

https://doi.org/10.1021/acsami.1c16464
ACS Appl. Mater. Interfaces 2021, 13, 57118−57131

methods reported previously.[19,20] The synthesis for Sc-TBAPy was performed in a 12 mL Pyrex reactor, where TBAPy (0.015 mmol, 10 mg) and $Sc(NO_3)_3{\cdot}xH_2O$ (0.03 mmol, 6.9 mg) were added to 4 mL of DMF/dioxane/H_2O mixture (2:1:1), followed by adding 10 μL of concentrated HNO_3. The suspension was sonicated for 15 min for the complete dissolution of the ligand. The reaction mixture was heated at 85 °C for 12 h, with a heating rate of 2 °C/min and then cooled to room temperature at a rate of 0.2 °C/min. The solid was recovered by centrifuge, and washed with DMF in order to remove any recrystallized TBAPy ligand. After drying, the as-made Sc-TBAPy MOF was obtained as a yellow solid powder. The peak indexation of Sc-TBAPy showed that the MOF has an orthorhombic unit cell with experimental cell parameters of a = 30.25(8) Å, b = 7.13(1) Å, and c = 15.32(4) Å, which are in agreement with the reported cell parameters of Ti-TBAPy and In-TBAPy.[20,21] Le Bail analysis of the collected powder pattern was carried out using TOPAS 5 software.[54] The profile fits confirmed that Sc-TBAPy is isostructural to the other M-TBAPy MOFs, with the space group of *Cmmm* (no. 65) (Figure S1). Thermogravimetric analysis reveals that the organic component of Sc-TBAPy decomposes at 500 °C (Figure S7a). Nitrogen adsorption–desorption analysis at 77 K showed that Sc-TBAPy has a Brunauer–Emmett–Teller (BET) surface area of 1197 $m^2\ g^{-1}$ (Figure S7b), which is close to those of Ti-TBAPy (1212 $m^2\ g^{-1}$)[21] and In-TBAPy (1189 $m^2\ g^{-1}$).[20]

For the synthesis of Sc-2, the same amounts of TBAPy (0.015 mmol, 10 mg) and $Sc(NO_3)_3{\cdot}xH_2O$ (0.03 mmol, 6.9 mg) were added to 4 mL of DMF/dioxane/H_2O mixture (2:1:1), followed by adding 10 μL of concentrated HNO_3 and 4.38 mg of CTAB. In the case of Sc-3, all the amounts remained the same except from the modulator (HNO_3), which is excluded from the synthesis. The suspensions were sonicated for 15 min for the complete dissolution of the ligand. The reaction mixtures were heated at 120 °C for 72 h, with a heating rate of 2 °C/min and then cooled to room temperature at a rate of 0.2 °C/min. Yellow powder samples were recovered by centrifuge and washed with DMF in order to remove any recrystallized TBAPy ligand.

Computational Details. The periodic structures of M-TBAPy (M = Al, In, Sc, and Ti) MOFs were optimized using the 65 space group (*Cmmm*) symmetry in CRYSTAL17 code.[55] All the structures were optimized using the PBE0 XC functional along with D3BJ dispersion corrections. Likewise, we further optimized the atomic coordinates of the structures considering the rotation of the benzene groups in the MOFs. Double-ζ basis set pob-DZVP was used to describe the organic atoms, while triple-ζ pop-TZVP basis was used to describe the metal atoms. The shrinking factors for the diagonalization of the Kohn–Sham matrix in the reciprocal space have been set to 4 for the Monkhorst–Pack and 4 for the Gilat nets. Band structure calculations were computed using the reciprocal space path within the first Brillouin zone in the primitive cell using the Seek-path package[56] using the primitive cell.

The study of the optical excitations and electron polarons in the periodic structures was performed in the CP2K code.[57] All structures were optimized initially with the PBE functional, followed by second optimization using the PBE0 exchange and correlation (XC) functional with the D3BJ dispersion correction in both cases. The double-ζ polarization MOLOPT basis sets were used to describe organic atoms, while a triple-ζ was used for metal atoms. The PBE0 calculations used the auxiliary MOLOPT-ADMM basis functions: cFIT8 for Al, cFIT12 for In, Sc, and Ti, and pFIT3 for nonmetal atoms. The Truncated Coulomb operator with a long-range correction was employed for the Hartree–Fock exchange of hybrid calculations. Both symmetric and rotated phenyl structures were considered as well using a 1 × 3 × 1 super cell of the conventional cell and a 4 × 1 × 1 of the primitive cell, respectively. The use of the 2 × 2 × 2 Monkhorst–Pack scheme in the initial PBE optimation guarantees the symmetrical orientation of the phenyl groups as a starting point for the PBE0 optimizations. On the other hand, the starting configuration of the rotated structure for the PBE0 optimization is obtained by rotating the phenyl groups and without the use of K-points during the PBE optimization. The truncation radius is half of the smallest edge of the unit cell (7.5 Å), and the long-range part of the exchange is computed using the PBE exchange. All calculations conducted with PBE0 used the orbital transformation method. Electron polaron geometry calculations were conducted using 45% of Hartree–Fock in order to impose localization of the electron. The LR-TDDFT scheme including the Tamm–Dancoff approximation was used to predict the optical band gap of the systems. To align the conduction and valence band energies with vacuum, the methodology proposed by Butler et al.[58] was used to calculate the vacuum level in the periodic systems. This method consists of evaluating the average potential within a small sphere at the pore center.

Water-framework interactions in each framework were studied with MD simulations in the canonical (*NVT*) ensemble at 298 K using the LAMMPS molecular software package.[59] The temperature of the systems was regulated using the Nosé-Hoover thermostat. Only one water molecule was simulated in each framework so that water–water interactions were avoided as the focus was only on how water interacts with the frameworks. Each system was equilibrated for 10 ns and then simulated for at least 100 ns using a timestep of 1 fs producing trajectories of the water dynamics. van der Waals interactions were modeled using a Lennard-Jones potential with a cutoff of 12.5 Å. The framework atoms were treated as flexible throughout the simulation where the universal force field[60] parameters were used for bonded and nonbonded interactions, and partial charges were computed with the REPEAT method[61] as implemented in the CP2K code[57] by using the PBE0 functional. The water molecules were modeled with the TIP4P2005[62] force field. Lorentz–Berthelot mixing rules were applied for dissimilar atomic interactions and Coulomb interactions were computed using Ewald summation. In addition to the simulations carried out with the flexible framework, the water distribution in a fixed framework, Al-TBAPy, was also modeled in order to investigate whether a less computationally demanding fixed framework simulation could be a reasonable approximation for this system. For this system, 100 water molecules were deposited to the system to improve statistics, while the water–water interactions were turned off, mimicking a single water particle simulation. From the water trajectories collected during the production runs, a three-dimensional probability grid was constructed by binning the number of times the water oxygen atom visited the volume of the respective grid point (0.2 Å × 0.2 Å × 0.2 Å). Potential energy surfaces were then created from the probability grids according to Boltzmann distribution and presented relative the minimum energy value. These are shown for the four respective structures at an isovalue of 15 kJ/mol. From these plots, we can identify three distinct adsorption sites. These sites are within the large pore (site 1), small pore (site 2), and between the pyrene stacking (site 3). We also calculated the probabilities of having a water molecule in the different binding sites in order to quantify the differences between the structures. For this, we used the TuTraSt algorithm[63] designed to partition potential energy grids into basins and transition states.

■ ASSOCIATED CONTENT

Supporting Information

The Supporting Information is available free of charge at https://pubs.acs.org/doi/10.1021/acsami.1c16464.

Experimental methods, calculation of AQY, photoluminescence spectra of M-TBAPy MOFs, computational details, band structure calculations, electron polarons in M-TBAPy MOFs, and water adsorption probabilities in M-TBAPy MOFs (PDF)

■ AUTHOR INFORMATION

Corresponding Author

Berend Smit − *Laboratory of Molecular Simulation (LSMO), Institut des Sciences et Ingénierie Chimiques (ISIC), Ecole Polytechnique Fédérale de Lausanne (EPFL), Sion CH-1951,*

https://doi.org/10.1021/acsami.1c16464
ACS Appl. Mater. Interfaces 2021, 13, 57118−57131

Switzerland; orcid.org/0000-0003-4653-8562; Email: berend.smit@epfl.ch

Authors

F. Pelin Kinik – *Laboratory of Molecular Simulation (LSMO), Institut des Sciences et Ingénierie Chimiques (ISIC), Ecole Polytechnique Fédérale de Lausanne (EPFL), Sion CH-1951, Switzerland;* orcid.org/0000-0002-2923-2679

Andres Ortega-Guerrero – *Laboratory of Molecular Simulation (LSMO), Institut des Sciences et Ingénierie Chimiques (ISIC), Ecole Polytechnique Fédérale de Lausanne (EPFL), Sion CH-1951, Switzerland;* orcid.org/0000-0002-0065-0623

Fatmah Mish Ebrahim – *Laboratory of Molecular Simulation (LSMO), Institut des Sciences et Ingénierie Chimiques (ISIC), Ecole Polytechnique Fédérale de Lausanne (EPFL), Sion CH-1951, Switzerland*

Christopher P. Ireland – *Laboratory of Molecular Simulation (LSMO), Institut des Sciences et Ingénierie Chimiques (ISIC), Ecole Polytechnique Fédérale de Lausanne (EPFL), Sion CH-1951, Switzerland;* orcid.org/0000-0002-2436-3987

Ozge Kadioglu – *Laboratory of Molecular Simulation (LSMO), Institut des Sciences et Ingénierie Chimiques (ISIC), Ecole Polytechnique Fédérale de Lausanne (EPFL), Sion CH-1951, Switzerland*

Amber Mace – *Department of Chemistry—Ångström Laboratory, Uppsala University, Uppsala SE-751 21, Sweden*

Mehrdad Asgari – *Laboratory of Molecular Simulation (LSMO), Institut des Sciences et Ingénierie Chimiques (ISIC), Ecole Polytechnique Fédérale de Lausanne (EPFL), Sion CH-1951, Switzerland*

Complete contact information is available at: https://pubs.acs.org/10.1021/acsami.1c16464

Author Contributions

[§]F.P.K. and A.O.-G. contributed equally to this work.

Notes

The authors declare no competing financial interest.

■ ACKNOWLEDGMENTS

This work was supported by the funding from the European Research Council (ERC) under the European Union's Horizon 2020 research and innovation programme (grant agreement no 666983, MaGic) and the Swiss National Science Foundation (SNSF) under grant 200021_172759. Calculations were performed at the EPFL High Performance Computer Center SCITAS and at the Swiss National Supercomputing Centre (CSCS) under project ID s1005. A.M. is thankful for the support for Swedish National Strategic e-Science programme (eSSENCE). The MD simulations were performed on resources provided by the Swedish National Infrastructure for Computing (SNIC) at NSC. We thank Dr. Maria Fumanal for helpful discussions.

■ REFERENCES

(1) Lee, J.; Farha, O. K.; Roberts, J.; Scheidt, K. A.; Nguyen, S. T.; Hupp, J. T. Metal–Organic Framework Materials as Catalysts. *Chem. Soc. Rev.* **2009**, *38*, 1450–1459.

(2) Gascon, J.; Corma, A.; Kapteijn, F.; Llabrés i Xamena, F. X. Metal Organic Framework Catalysis: Quo Vadis? *ACS Catal.* **2014**, *4*, 361–378.

(3) Doonan, C. J.; Sumby, C. J. Metal–Organic Framework Catalysis. *CrystEngComm* **2017**, *19*, 4044–4048.

(4) Chen, Y.-Z.; Zhang, R.; Jiao, L.; Jiang, H.-L. Metal–Organic Framework-Derived Porous Materials for Catalysis. *Coord. Chem. Rev.* **2018**, *362*, 1–23.

(5) Wei, Y.-S.; Zhang, M.; Zou, R.; Xu, Q. Metal–Organic Framework-Based Catalysts with Single Metal Sites. *Chem. Rev.* **2020**, *120*, 12089–12174.

(6) Li, X.; Wang, Z.; Wang, L. Metal–Organic Framework-Based Materials for Solar Water Splitting. *Small Sci.* **2021**, *1*, 2000074.

(7) Lee, J. G.; Nam, E.; An, K. Modified Metal–Organic Frameworks as Efficient Catalysts for Lignocellulosic Biomass Conversion. *Bull. Korean Chem. Soc.* **2021**, *42*, 346–358.

(8) Liu, S.; Zhang, C.; Sun, Y.; Chen, Q.; He, L.; Zhang, K.; Zhang, J.; Liu, B.; Chen, L.-F. Design of Metal–Organic Framework-Based Photocatalysts for Hydrogen Generation. *Coord. Chem. Rev.* **2020**, *413*, 213266.

(9) Zhu, B.; Zou, R.; Xu, Q. Metal–Organic Framework Based Catalysts for Hydrogen Evolution. *Adv. Energy Mater.* **2018**, *8*, 1801193.

(10) Xiao, J.-D.; Jiang, H.-L. Metal–Organic Frameworks for Photocatalysis and Photothermal Catalysis. *Acc. Chem. Res.* **2018**, *52*, 356–366.

(11) Tasleem, S.; Tahir, M.; Khalifa, W. A. Current Trends in Structural Development and Modification Strategies for Metal–Organic Frameworks (MOFs) Towards Photocatalytic H_2 Production: A Review. *Int. J. Hydrogen Energy* **2021**, *46*, 14148–14189.

(12) Ohtani, B. Photocatalysis A to Z – What We Know and What We Do Not Know in a Scientific Sense. *J. Photochem. Photobiol., C* **2010**, *11*, 157–178.

(13) Wang, W.; Xu, X.; Zhou, W.; Shao, Z. Recent Progress in Metal–Organic Frameworks for Applications in Electrocatalytic and Photocatalytic Water Splitting. *Adv. Sci.* **2017**, *4*, 1600371.

(14) Zhao, C.; Chen, Z.; Shi, R.; Yang, X.; Zhang, T. Recent Advances in Conjugated Polymers for Visible-Light-Driven Water Splitting. *Adv. Mater.* **2020**, *32*, 1907296.

(15) Guo, F.; Guo, J.-H.; Wang, P.; Kang, Y.-S.; Liu, Y.; Zhao, J.; Sun, W.-Y. Facet-Dependent Photocatalytic Hydrogen Production of Metal–Organic Framework NH_2-MIL-125(Ti). *Chem. Sci.* **2019**, *10*, 4834–4838.

(16) Nasalevich, M. A.; Hendon, C. H.; Santaclara, J. G.; Svane, K.; Van Der Linden, B.; Veber, S. L.; Fedin, M. V.; Houtepen, A. J.; Van Der Veen, M. A.; Kapteijn, F.; Walsh, A.; Gascon, J. Electronic Origins of Photocatalytic Activity in d^0 Metal Organic Frameworks. *Sci. Rep.* **2016**, *6*, 23676.

(17) Figueira-Duarte, T. M.; Müllen, K. Pyrene-Based Materials for Organic Electronics. *Chem. Rev.* **2011**, *111*, 7260–7314.

(18) Kinik, F. P.; Ortega-Guerrero, A.; Ongari, D.; Ireland, C. P.; Smit, B. Pyrene-Based Metal Organic Frameworks: From Synthesis to Applications. *Chem. Soc. Rev.* **2021**, *50*, 3143–3177.

(19) Boyd, P. G.; Chidambaram, A.; García-Díez, E.; Ireland, C. P.; Daff, T. D.; Bounds, R.; Gładysiak, A.; Schouwink, P.; Moosavi, S. M.; Maroto-Valer, M. M.; Reimer, J. A.; Navarro, J. A. R.; Woo, T. K.; Garcia, S.; Stylianou, K. C.; Smit, B. Data-Driven Design of Metal–Organic Frameworks for Wet Flue Gas CO_2 Capture. *Nature* **2019**, *576*, 253–256.

(20) Stylianou, K. C.; Heck, R.; Chong, S. Y.; Bacsa, J.; Jones, J. T. A.; Khimyak, Y. Z.; Bradshaw, D.; Rosseinsky, M. J. A Guest-Responsive Fluorescent 3D Microporous Metal–Organic Framework Derived from a Long-Lifetime Pyrene Core. *J. Am. Chem. Soc.* **2010**, *132*, 4119–4130.

(21) Cadiau, A.; Kolobov, N.; Srinivasan, S.; Goesten, M. G.; Haspel, H.; Bavykina, A. V.; Tchalala, M. R.; Maity, P.; Goryachev, A.; Poryvaev, A. S.; Eddaoudi, M.; Fedin, M. V.; Mohammed, O. F.; Gascon, J. A Titanium Metal–Organic Framework with Visible-Light-Responsive Photocatalytic Activity. *Angew. Chem.* **2020**, *132*, 13570–13574.

(22) Wang, S.; Reinsch, H.; Heymans, N.; Wahiduzzaman, M.; Martineau-Corcos, C.; De Weireld, G.; Maurin, G.; Serre, C. Toward

a Rational Design of Titanium Metal−Organic Frameworks. *Matter* **2020**, *2*, 440−450.
(23) Nguyen, H. L. Perspectives on Titanium-Based Metal−Organic Frameworks. *J. Phys. Energy* **2021**, *3*, 021003.
(24) Xie, L. S.; Skorupskii, G.; Dincă, M. Electrically Conductive Metal−Organic Frameworks. *Chem. Rev.* **2020**, *120*, 8536−8580.
(25) Fumanal, M.; Ortega-Guerrero, A.; Jablonka, K. M.; Smit, B.; Tavernelli, I. Charge Separation and Charge Carrier Mobility in Photocatalytic Metal-Organic Frameworks. *Adv. Funct. Mater.* **2020**, *30*, 2003792.
(26) Muschielok, C.; Oberhofer, H. Aspects of Semiconductivity in Soft, Porous Metal−Organic Framework Crystals. *J. Chem. Phys.* **2019**, *151*, 015102.
(27) Ortega-Guerrero, A.; Fumanal, M.; Capano, G.; Smit, B. From Isolated Porphyrin Ligands to Periodic Al-PMOF: A Comparative Study of the Optical Properties Using DFT/TDDFT. *J. Phys. Chem. C* **2020**, *124*, 21751−21760.
(28) Patwardhan, S.; Schatz, G. C. Theoretical Investigation of Charge Transfer in Metal Organic Frameworks for Electrochemical Device Applications. *J. Phys. Chem. C* **2015**, *119*, 24238−24247.
(29) Ortega-Guerrero, A.; Fumanal, M.; Capano, G.; Tavernelli, I.; Smit, B. Insights into the Electronic Properties and Charge Transfer Mechanism of a Porphyrin Ruthenium-Based Metal−Organic Framework. *Chem. Mater.* **2020**, *32*, 4194−4204.
(30) Capano, G.; Ambrosio, F.; Kampouri, S.; Stylianou, K. C.; Pasquarello, A.; Smit, B. On the Electronic and Optical Properties of Metal−Organic Frameworks: Case Study of MIL-125 and MIL-125-NH_2. *J. Phys. Chem. C* **2020**, *124*, 4065−4072.
(31) Ghosh, D.; Welch, E.; Neukirch, A. J.; Zakhidov, A.; Tretiak, S. Polarons in Halide Perovskites: A Perspective. *J. Phys. Chem. Lett.* **2020**, *11*, 3271−3286.
(32) Braslavsky, S. E. Glossary of Terms Used in Photochemistry, (IUPAC Recommendations 2006). *Pure Appl. Chem.* **2007**, *79*, 293−465.
(33) Hatchard, C.; Parker, C. A. A New Sensitive Chemical Actinometer-II. Potassium Ferrioxalate as a Standard Chemical Actinometer. *Proc. R. Soc. A* **1956**, *235*, 518−536.
(34) Kuhn, H. J.; Braslavsky, S. E.; Schmidt, R. Chemical Actinometry (IUPAC Technical Report). *Pure Appl. Chem.* **2004**, *76*, 2105−2146.
(35) Kampouri, S.; Nguyen, T. N.; Ireland, C. P.; Valizadeh, B.; Ebrahim, F. M.; Capano, G.; Ongari, D.; Mace, A.; Guijarro, N.; Sivula, K.; Sienkiewicz, A.; Forró, L.; Smit, B.; Stylianou, K. C. Photocatalytic Hydrogen Generation from a Visible-Light Responsive Metal−Organic Framework System: The Impact of Nickel Phosphide Nanoparticles. *J. Mater. Chem. A* **2018**, *6*, 2476−2481.
(36) Caballero-Mancebo, E.; Cohen, B.; Smolders, S.; De Vos, D. E.; Douhal, A. Unravelling Why and to What Extent the Topology of Similar Ce-Based MOFs Conditions their Photodynamic: Relevance to Photocatalysis and Photonics. *Adv. Sci.* **2019**, *6*, 1901020.
(37) Wang, G.; Sun, Q.; Liu, Y.; Huang, B.; Dai, Y.; Zhang, X.; Qin, X. A Bismuth-Based Metal−Organic Framework as an Efficient Visible-Light-Driven Photocatalyst. *Chem.—Eur. J.* **2015**, *21*, 2364−2367.
(38) Zhang, J.; Bai, T.; Huang, H.; Yu, M. H.; Fan, X.; Chang, Z.; Bu, X. H. Metal−Organic-Framework-Based Photocatalysts Optimized by Spatially Separated Cocatalysts for Overall Water Splitting. *Adv. Mater.* **2020**, *32*, 2004747.
(39) Berera, R.; van Grondelle, R.; Kennis, J. T. M. Ultrafast Transient Absorption Spectroscopy: Principles and Application to Photosynthetic Systems. *Photosynth. Res.* **2009**, *101*, 105−118.
(40) Miyasaka, H.; Masuhara, H.; Mataga, N. Picosecond Absorption Spectra and Relaxation Processes of the Excited Singlet State of Pyrene in Solution. *Laser Chem.* **1983**, *1*, 357−386.
(41) Foggi, P.; Pettini, L.; Santa, I.; Righini, R.; Califano, S. Transient Absorption and Vibrational Relaxation Dynamics of the Lowest Excited Singlet State of Pyrene in Solution. *J. Phys. Chem. C* **1995**, *99*, 7439−7445.
(42) Gładysiak, A.; Nguyen, T. N.; Bounds, R.; Zacharia, A.; Itskos, G.; Reimer, J. A.; Stylianou, K. C. Temperature-Dependent Interchromophoric Interaction in a Fluorescent Pyrene-Based Metal−Organic Framework. *Chem. Sci.* **2019**, *10*, 6140−6148.
(43) Kawakami, T.; Koga, M.; Sotome, H.; Miyasaka, H. Ultrafast Capture of Electrons Ejected by Photoionization Leading to the Formation of a Charge-Separated State at a High Energy Level. *Phys. Chem. Chem. Phys.* **2020**, *22*, 17472−17481.
(44) Sarkisov, L.; Martin, R. L.; Haranczyk, M.; Smit, B. On the Flexibility of Metal−Organic Frameworks. *J. Am. Chem. Soc.* **2014**, *136*, 2228−2231.
(45) Rogge, S. M. J.; Waroquier, M.; Van Speybroeck, V. Reliably Modeling the Mechanical Stability of Rigid and Flexible Metal−Organic Frameworks. *Acc. Chem. Res.* **2018**, *51*, 138−148.
(46) Dhakshinamoorthy, A.; Li, Z.; Garcia, H. Catalysis and Photocatalysis by Metal Organic Frameworks. *Chem. Soc. Rev.* **2018**, *47*, 8134−8172.
(47) Kampouri, S.; Nguyen, T. N.; Spodaryk, M.; Palgrave, R. G.; Züttel, A.; Smit, B.; Stylianou, K. C. Concurrent Photocatalytic Hydrogen Generation and Dye Degradation Using MIL-125-NH_2 under Visible Light Irradiation. *Adv. Funct. Mater.* **2018**, *28*, 1806368.
(48) Cheng, X.-M.; Dao, X.-Y.; Wang, S.-Q.; Zhao, J.; Sun, W.-Y. Enhanced Photocatalytic CO_2 Reduction Activity over NH_2-MIL-125(Ti) by Facet Regulation. *ACS Catal.* **2020**, *11*, 650−658.
(49) Guo, F.; Yang, S.; Liu, Y.; Wang, P.; Huang, J.; Sun, W.-Y. Size Engineering of Metal−Organic Framework MIL-101(Cr)−Ag Hybrids for Photocatalytic CO_2 Reduction. *ACS Catal.* **2019**, *9*, 8464−8470.
(50) Liu, L.; Han, Z.-B.; Wang, S.-M.; Yuan, D.-Q.; Ng, S. W. Robust Molecular Bowl-Based Metal−Organic Frameworks with Open Metal Sites: Size Modulation To Increase the Catalytic Activity. *Inorg. Chem.* **2015**, *54*, 3719−3721.
(51) Wang, W.-N.; An, W.-J.; Ramalingam, B.; Mukherjee, S.; Niedzwiedzki, D. M.; Gangopadhyay, S.; Biswas, P. Size and Structure Matter: Enhanced CO_2 Photoreduction Efficiency by Size-Resolved Ultrafine Pt Nanoparticles on TiO_2 Single Crystals. *J. Am. Chem. Soc.* **2012**, *134*, 11276−11281.
(52) Liu, Y.; Gao, P.; Huang, C.; Li, Y. Shape-and Size-Dependent Catalysis Activities of Iron-Terephthalic Acid Metal−Organic Frameworks. *Sci. China Chem.* **2015**, *58*, 1553−1560.
(53) Wang, T. C.; Vermeulen, N. A.; Kim, I. S.; Martinson, A. B. F.; Stoddart, J. F.; Hupp, J. T.; Farha, O. K. Scalable Synthesis and Post-Modification of a Mesoporous Metal−Organic Framework Called NU-1000. *Nat. Protoc.* **2016**, *11*, 149−162.
(54) Coelho, A. A. TOPAS and TOPAS-Academic: An Optimization Program Integrating Computer Algebra and Crystallographic Objects Written in C++. *J. Appl. Crystallogr.* **2018**, *51*, 210−218.
(55) Dovesi, R.; Erba, A.; Orlando, R.; Zicovich-Wilson, C. M.; Civalleri, B.; Maschio, L.; Rérat, M.; Casassa, S.; Baima, J.; Salustro, S.; Kirtman, B. Quantum-Mechanical Condensed Matter Simulations with CRYSTAL. *Wiley Interdiscip. Rev.: Comput. Mol. Sci.* **2018**, *8*, 1360.
(56) Hinuma, Y.; Pizzi, G.; Kumagai, Y.; Oba, F.; Tanaka, I. Band Structure Diagram Paths Based on Crystallography. *Comput. Mater. Sci.* **2017**, *128*, 140−184.
(57) Kühne, T. D.; et al. CP2K: An Electronic Structure and Molecular Dynamics Software Package - Quickstep: Efficient and Accurate Electronic Structure Calculations. *J. Chem. Phys.* **2020**, *152*, 194103.
(58) Butler, K. T.; Hendon, C. H.; Walsh, A. Electronic Chemical Potentials of Porous Metal−Organic Frameworks. *J. Am. Chem. Soc.* **2014**, *136*, 2703−2706.
(59) Plimpton, S. Fast Parallel Algorithms for Short-Range Molecular Dynamics. *J. Comput. Phys.* **1995**, *117*, 1−19.
(60) Rappe, A. K.; Colwell, K. S.; Casewit, C. J. Application of a Universal Force Field to Metal Complexes. *Inorg. Chem.* **1993**, *32*, 3438−3450.

https://doi.org/10.1021/acsami.1c16464
ACS Appl. Mater. Interfaces 2021, 13, 57118−57131

(61) Campañá, C.; Mussard, B.; Woo, T. K. Electrostatic Potential Derived Atomic Charges for Periodic Systems Using a Modified Error Functional. *J. Chem. Theory Comput.* **2009**, *5*, 2866−2878.
(62) Abascal, J. L. F.; Vega, C. A General Purpose Model for the Condensed Phases of Water: TIP4P/2005. *J. Chem. Phys.* **2005**, *123*, 234505.
(63) Mace, A.; Barthel, S.; Smit, B. Automated Multiscale Approach To Predict Self-Diffusion from a Potential Energy Field. *J. Chem. Theory Comput.* **2019**, *15*, 2127−2141.

https://doi.org/10.1021/acsami.1c16464
ACS Appl. Mater. Interfaces 2021, 13, 57118−57131